Generalization of the Dark Channel Prior for Single Image Restoration

Publisher: IEEE

Cite This

3 Author(s) Yan-Tsung Peng ; Keming Cao ; Pamela C. Cosman **View All Authors**

Down PDF

Abstract: Images degraded by light scattering and absorption, such as hazy, sandstorm, and underwater images, often suffer color distortion and low contrast because of light travel... **View more**

Metadata

Abstract:
Images degraded by light scattering and absorption, such as hazy, sandstorm, and underwater images, often suffer color distortion and low contrast because of light traveling through turbid media. In order to enhance and restore such images, we first estimate ambient light using the depth-dependent color change. Then, via calculating the difference between the observed intensity and the ambient light, which we call the scene ambient light differential, scene transmission can be estimated. Additionally, adaptive color correction is incorporated into the image formation model (IFM) for removing color casts while restoring contrast. Experimental results on various degraded images demonstrate the new method outperforms other IFM-based methods subjectively and objectively. Our approach can be interpreted as a generalization of the common dark channel prior (DCP) approach to image restoration, and our method reduces to several DCP variants for different special cases of ambient lighting and turbid medium conditions.

Published in: IEEE Transactions on Image Processing (Volume: 27 , Issue: 6 , June 2018)

Page(s): 2856 - 2868

INSPEC Accession Number: 17630407

Date of Publication: 07 March 2018

DOI: 10.1109/TIP.2018.2813092

ISSN Information:

Publisher: IEEE

Funding Agency:

SECTION I.
Introduction

Images or videos captured in different conditions sometimes suffer from visibility degradation because light is scattered and absorbed with distance from the camera through turbid media, such as fog, haze, sandstorms, or water. The degradation reduces the visual quality of the images and videos and affects the performance of computer vision applications. Thus, developing an effective method to restore color and contrast for such images is desirable. Fig. 1(a)-(e) shows five different images degraded by light scattering and absorption.

Fig. 1.
(a)–(e) Examples of different images degraded by light scattering and absorption. The original image (a) is from [1], (b) is from [4], (c) is from [37] (d) is from [21] and (e) is from [38].

There has been much research [1]–[2][3][4][5] on image defogging and visibility restoration using the image formation model (IFM) [6]. Fig. 2 shows how an image is described using the IFM [6]–[7][8]. Here $I^c(x)$, the observed intensity at pixel x , consists of the scene radiance $J^c(x)$ blended with the ambient light A^c according to the transmission map $t(x)$, where c is one of the red, green, and blue channels. The transmission describes the portion of the scene radiance which is not scattered or absorbed and which reaches the camera. Thus, a larger value in the transmission map means that the corresponding scene point is closer to the camera.

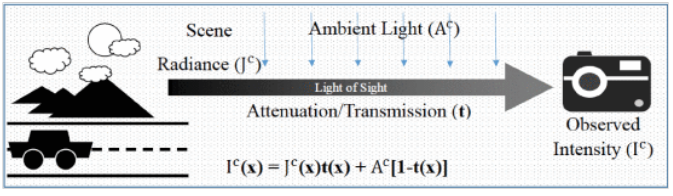

Fig. 2.
Image formation model.

Using the IFM, He *et al.* [1] presented the dark channel prior (DCP) to remove fog/haze in natural terrestrial images via estimation of the ambient light and transmission. This motivated many image restoration approaches [2]–[3][4][5], [9]–[10][11][12][13][14][15][16] that improve and extend the DCP for different goals and applications. However, haze with different color casts may lead to under- or over-estimated transmission based on the DCP, causing poor restoration results. In [4] and [5], restoration methods for hazy and sandstorm images were presented; they used adaptive gamma correction to solve the transmission over-estimation caused by the low observed intensity due to color casts, and adopted color correction to compensate for the color cast. Nevertheless, the underlying reason for inaccurate transmission estimation for images with color casts is that the DCP is not as reliable for such images as for those without color casts. This problem often cannot be solved only by gamma correction. Hence, these methods are unable to restore heavily tinted sandstorm images because most blue light is scattered and absorbed, which causes the DCP to fail and leads to inaccurate ambient light and transmission estimation. In order to estimate medium transmission more precisely, some researchers

exploited learning algorithms to generate a mapping function where the input is a hazy image, and the output is its depth map [17]–[18][19]. However, these methods only consider hazy images that have bright ambient light and no color cast, and are often unable to restore more general hazy images with different lighting conditions and color tones.

Several studies also have been conducted on restoring underwater images based on the DCP [9]–[10][11], [14], [15] or its variants [12], [13]. However, measuring transmission for underwater images based on the DCP [9]–[10][11], [14] frequently fails to generate accurate results since red light is more attenuated than other wavelengths underwater, and thus the DCP based on RGB channels ends up considering only the red channel, causing unreliable transmission estimation. Several DCP variants consider only the green and blue channels [12], the RGB channels with the red inverted [13], or the minimal information loss principle (MILP) [15] to try to estimate transmission underwater, but they may still fail due to different underwater lighting conditions and color tones. Instead of using the DCP, the maximum intensity prior (MIP) approach [16] calculates the difference between the maximum intensity of the red channel and that of the green and blue channels to estimate transmission. However, these methods frequently perform poorly as the light absorption and lighting conditions that exist in underwater images invalidate these priors. For example, all the DCP-, MIP-, and MILP-based restoration methods are unable to restore underwater images with dim ambient light, where the background pixels are dark and would be wrongly judged as being close.

In this paper, we improve DCP-based image restoration using a new approach to estimating ambient light (which is needed by the DCP restoration methods), and using adaptive color correction incorporated into the IFM. The method can be applied to enhancing and restoring foggy, hazy, sandstorm, and underwater images, including both well-lit and dimly lit images. The algorithmic contributions of this work, compared to [22], include the depth-dependent color change for estimating ambient light for a wide range of degraded images, and adaptive color correction in the IFM. We demonstrate that our approach is a generalization of the DCP, and we present both subjective and objective experimental results.

The rest of the paper is organized as follows. In Section II, we review DCP-based image restoration [1] and its limitations. Section III details the new method. Section IV reports experimental results, and Section V summarizes the conclusions.

SECTION II.
Enhancement and Restoration Based on DCP

In this section, we review dehazing based on the DCP [1], which was broadly adopted and improved to apply to hazy, sandstorm, and underwater images [2]–[3][4][5], [9]–[10][11][12][13][14]. Assuming that light attenuation is homogeneous, the IFM [6] is given by:

$$I^c(x) = J^c(x)t(x) + A^c\big(1 - t(x)\big), \quad c \in \{r, g, b\} \tag{1}$$

View Source

where $I^c(x)$ is the observed intensity in color channel c at pixel x, J^c is the scene radiance, A^c is the ambient light, and t is the transmission, where c is one of the RGB channels. Note that we assume I^c, J^c, and $A^c \in [0, 1]$.

For each pixel x in an image, the DCP finds the minimum value among RGB channels in a local patch $\Omega(x)$ centered at x, that is:

$$\tilde{t}^{rgb}_{dcp}(x) = \min_{y \in \Omega(x)} \left\{ \min_{c \in \{r,g,b\}} I^c(y) \right\}, \quad \text{for an outdoor daytime}$$

haze-free image, J_{dcp}^{rgb} is often close to zero, because at least one of the three color channels will typically have a low-intensity pixel in the local patch in $\Omega(x)$. It was asserted in [4, eq. (9)] that $J_{dcp}^{rgb} = 0$ for about 75% of non-sky pixels in haze-free images.

Dividing both sides of Eq. (1) by A^c and applying the minimum operators to it, the term involving J^c is dropped as being close to zero, and the transmission estimate $\tilde{t}_{rgb}(x) = \min_{y\in\Omega(x)} t(y)$, described in [4, eq. (11)], is

$$\tilde{t}_{rgb}(x) = 1 - \min_{y\in\Omega(x)} \left\{ \min_{c\in\{r,g,b\}} \frac{I^c(y)}{A^c} \right\}. \tag{2}$$

View Source

Since $\tilde{t}_{rgb}$ has block-like artifacts, it can be refined by median filtering [3], image matting [25], or guided filtering [26]. To estimate A^c , the DCP for a hazy image is calculated as:

$$I_{dcp}^{rgb}(x) = \min_{y\in\Omega(x)} \left\{ \min_{c\in\{r,g,b\}} I^c(y) \right\}. \tag{3}$$

View Source

For the DCP of a hazy image, far and close scene points, x_f and x_c , generally have $I_{dcp}^{rgb}(x_c) \leq I_{dcp}^{rgb}(x_f)$ because of scattered light. Therefore, I_{dcp}^{rgb} provides depth information for hazy images. Based on I_{dcp}^{rgb} , ambient light A^c is selected from one of the farthest and haziest pixels in the input image. Let $P^{0.1\%}$ be the set of positions of the top 0.1% largest valued (assumed farthest) pixels in I_{dcp}^{rgb} . Among these pixels, the one with the highest intensity in the input image provides the estimate of ambient light A^c [1]:

$$A^c = I^c \left(\mathbf{argmax}_{x\in P^{0.1\%}} \sum_{c\in\{r,g,b\}} I^c(x) \right). \tag{4}$$

View Source

Finally, by putting I^c , $\tilde{t}_{rgb}$ and A^c into Eq. (1), the estimated scene radiance is calculated as:

$$J^c(x) = \frac{I^c(x) - A^c}{\max\left(\tilde{t}_{rgb}(x), t_0\right)} + A^c, \tag{5}$$

View Source

where t_0 is empirically set in the range [0.1, 0.4] to increase the exposure of J^c for display.

In general, the DCP-based methods are based on three assumptions made for hazy terrestrial images: overcast lighting, spatially invariant attenuation coefficients, and wavelength-independent attenuation. Sandstorm and underwater images have different possible lighting conditions and color casts, which may violate the assumptions underlying these priors, producing poor restoration results. For example, red light is strongly abosorbed underwater, so small values in the red channel make the DCP values of a far scene small, causing inaccurate image depth and ambient light estimation (e.g., Fig. 3(d)). Therefore, several DCP variants [12], [13], [23], [24] were created for ambient light and transmission estimation with different lighting conditions and color casts, shown in Table I and Table II.

TABLE I Formulas for Estimation of Depth [1], [12], [13], [24]

TABLE II Formulas for Estimation of transmission [1], [12], [13], [24]

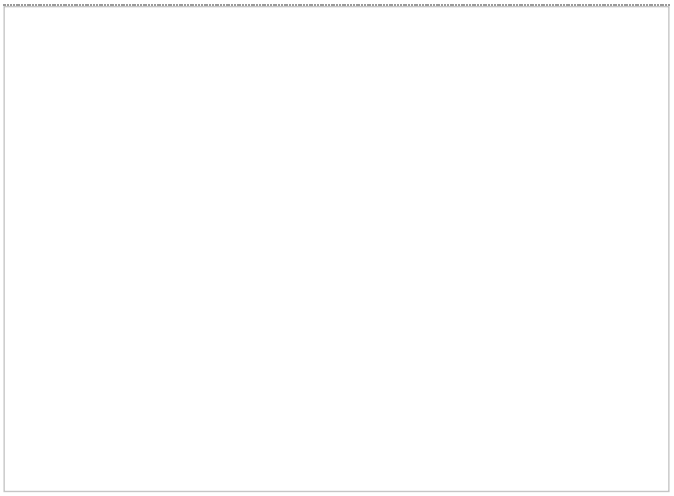

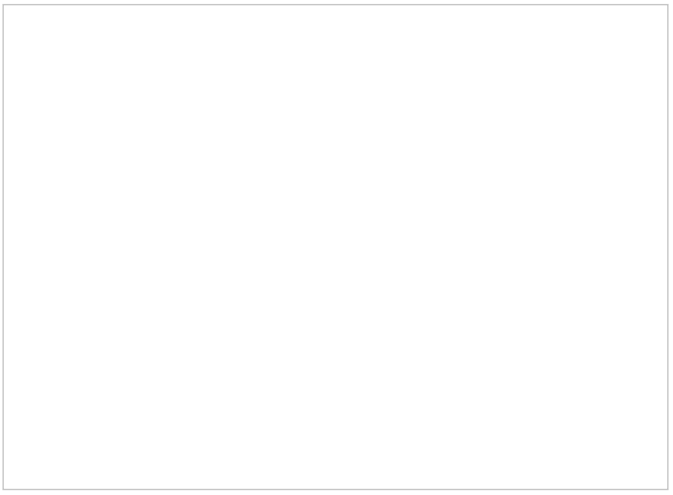

Fig. 3.
Examples of depth estimation via the DCP (I_{dcp}^{rgb}); (a) and (b) are successful cases while (c) and (d) are failure cases. The original images of (a), (b), and (d) come from [1], [38], and [16].

The original images in the first two columns of Fig. 3 have lighting conditions appropriate to the DCP-based methods. Dark foreground pixels cause the dark channel to have a small value, so they are correctly estimated as being close. The background lacks dark pixels, so these regions are correctly estimated to be relatively far away. By contrast, the DCP works poorly for the original images in the last two columns of Fig. 3. The sandstorm image has small values in the blue channel, so the DCP in Eq. (3) has small values everywhere coming from the blue channel, the entire scene is mistakenly judged as being very close. The underwater image in the fourth column was captured with artificial lights. The bright foreground is erroneously viewed as being far while the

dark background is incorrectly deemed to be close. In Section IV, we will show other examples where the DCP-based methods do not work properly because of different lighting conditions and color casts.

SECTION III.
Description of the Method

Fig. 4 depicts the overall flowchart of our method. The steps are explained in the following sections.

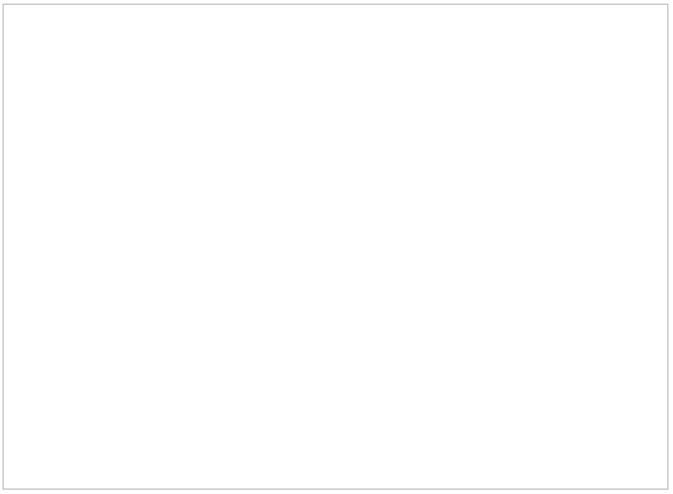

Fig. 4.
Overall flowchart of our method. The original image is from [5].

A. Ambient Light Estimation

We generalize the DCP based on the depth-dependent color change, which describes whether a given color channel tends to have larger or smaller values as depth from the camera increases. A three-bit indicator $\mathbf{s} = s_r s_g s_b$ is used, where $s_c = 1$ means that light for channel c tends to increase with depth, while $s_c = 0$ indicates that light for c tends to decrease, where $c \in \{r, g, b\}$. There are 8 different values for the indicator: $\mathbf{s} \in \{000, 001, \ldots, 111\}$. To determine the indicator for an image, we estimate a rough depth map D_r based on the observation that far scene points tend to have smoother regions (due to scattering) and so have smaller gradients than close scene points. A gradient map is first computed as $G(x) = \sqrt{G_h(x)^2 + G_v(x)^2}$, where G_h and G_v are the horizontal and vertical 3×3 Sobel operators applied to the input image. Assuming depth in a small local patch is uniform, a modified gradient map G_m is estimated by dilating G and filling holes [27]. Then, we set $D_r(x) = 1 - F_s(G_m(x))$, where F_s linearly stretches G_m to the range [0, 1].

The relationship between depth and I^c is modeled via regression: $\widehat{I^c}(x) = b_c + a_c \times D_r(x)$, where a_c and b_c are estimated using $\mathbf{argmin}_{a_c,b_c} \sum_x \left(I^c(x) - \widehat{I^c}(x)\right)^2$. The indicator s_c for channel c equals 1 if $a_c > 0$ and equals 0 otherwise, where $c \in \{r, g, b\}$. In addition, a larger $|a_c|$ means higher significance of the corresponding channel c to determine the scene depth. Rather than using Eq. (3) as the depth map estimate for purposes of estimating ambient light, we estimate the depth map D using the indicator $s_r s_g s_b$ and $|a_c|$ as:

$$D(x) = \min_{c, y \in \Omega(x)} \big(1 - w_c \mid s_c - I^c(y) \mid \big), \tag{6}$$

View Source

where $w_c = \tanh(k|a_c|)$ is the significance weighting factor for channel c , where $k = 4$ is an empirical constant. Here the function $\tanh(z) = \frac{e^z - e^{-z}}{e^z + e^{-z}}$ is the hyperbolic tangent.

Fig. 5 shows the flowchart of calculation of the depth-dependent color change. There are two main reasons why we chose to use linear regression for capturing correlation between RGB intensity values and scene depth. First, the linear fit is simple, and is sufficient for our purposes. Second, the error of the linear fit between RGB intensities and depth tends to be smaller when an accurate depth map is used. For example, the fit is much better in Fig. 6 where the RGB intensities of image I are plotted with the improved depth map D from Fig. 5. We also tried other color spaces but found the RGB color space to be the best fit for our method.

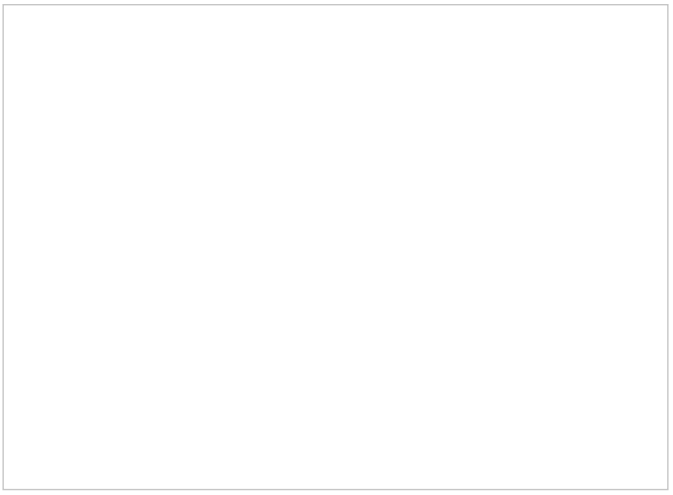

Fig. 5.
The flowchart of calculation of the depth-dependent color change.

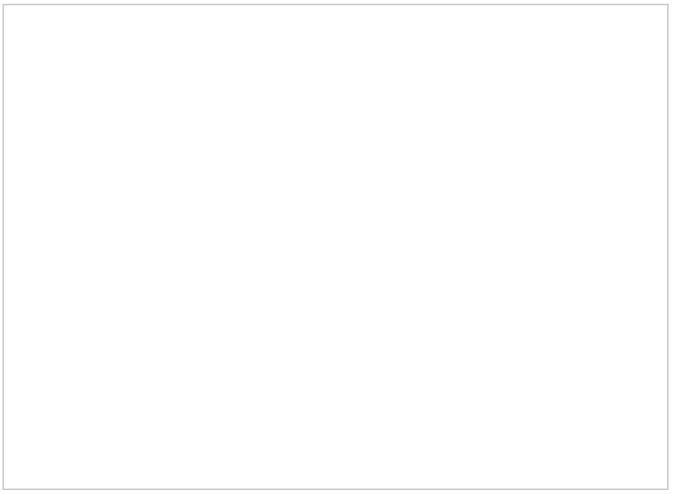

Fig. 6.
The regression analysis plot using image I and the improved depth map D from Fig. 5.

Using the indicator $\mathbf{s}$ and the significance weighting factors $\mathbf{w} = [w_r, w_g, w_b]$, we have developed a general formulation for DCP-based methods. The approach for hazy images [1], sandstorm images [4], [5], and some underwater images [9]–[10][11], two approaches for night-time terrestrial images [23], [24], and two approaches for underwater images [12], [13] are all special cases of Eq. (6), as will be discussed later.

Fig. 7 shows comparisons of depth estimation based on the DCP [1], DCP variants [12], [13], [24], and our depth estimation. Fig. 7(a) shows a hazy image and its estimated depth maps. I_{dcp}^{rgb} works for the hazy image since its $\mathbf{s}$ and $\mathbf{w}$ indicate that the values of all three color channels, which are all significant, tend to increase with depth. Fig. 7(b) shows an underwater image where both I_{dcp}^{rgb} and I_{dcp}^{gb} work since $\mathbf{s} = 111$ and $\mathbf{w}$ are similar to those for I^c in Fig. 7(a). However, the depth estimated using I_{dcp}^{rgb} is not accurate for Fig. 7(b), because its $s_r = 1$ means the

values of the red channel increase with depth but $I_{dcp}^{r'gb}$, which inverts the red channel, considers the red values decrease with increasing depth. The sandstorm image in Fig. 7(c) has small blue values, causing I_{dcp}^{rgb} to only consider the blue channel and to fail to produce a proper depth map. As can be seen in Fig. 7(d), $I_{dcp}^{r'gb}$ works well for the underwater image since red values tend to decrease and green and blue values tend to increase with depth based on its **s** while I_{dcp}^{rgb} , assuming an opposite tendency for red, does not work. I_{dcp}^{gb} works somewhat imprecisely (fish is wrongly judged as being far) because it does not consider the red channel. Fig. 7(e) and (f) show two underwater images with artificial lighting, for which I_{dcp}^{rgb}, I_{dcp}^{gb} and $I_{dcp}^{r'gb}$ all do poorly estimating the depth because none of them works when green values decrease with increasing depth. $I_{dcp}^{r'g'b'}$ works well when the values in all three color channels tend to decrease as the depth increases, such as the underwater image in Fig. 7(f) and the dimly-lit image in Fig. 7(g). Our method, which incorporates the depth-dependent color change indicators and significance weighting factors, is capable of generating proper depth maps for all of these degraded images with different color change and lighting conditions.

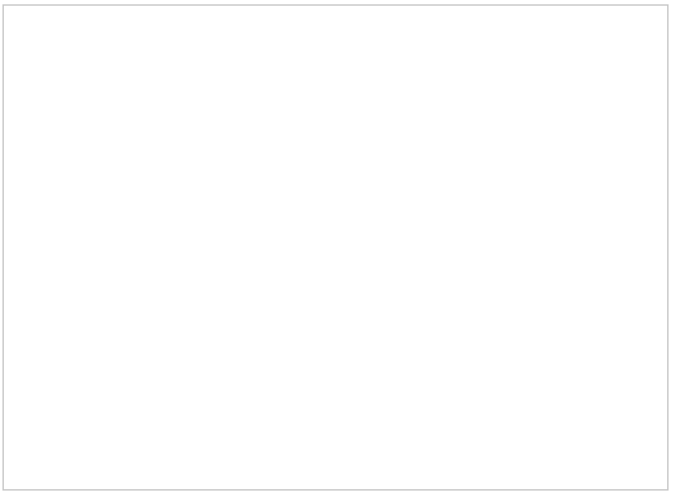

Fig. 7.
Comparisons of depth estimation based on the DCP [1], [4], [5], [9]–[10][11], DCP variants [12], [13], [24], and our method for images with different light lighting conditions and color casts. The first row of images shows (a) A hazy image with **s** = 111, (b) an underwater image with **s** = 111, (c) a sandstorm image with **s** = 111, (d)-(f) underwater images with **s** = 011, 001, 000, and (g) a dimly lit image with **s** = 000. The next four rows show the estimated depth images using various methods. The last row shows our depth images. The original image of (g) and depth images shown here undergo simple individual contrast stretching or scaling steps for display. Original images are taken from [1], [38], [37], [16], [39], and [44].

Ambient light is estimated from the input pixels corresponding to the top 0.1% farthest pixels in D :

$$A^c = \frac{1}{|P_D^{0.1\%}|} \sum_{x \in P_D^{0.1\%}} I^c(x), \tag{7}$$

View Source

where $P_D^{0.1\%}$ is the set of positions of the top 0.1% largest-valued pixels in D .

B. Scene Transmission Estimation

Transmission estimation based on scene ambient light differential was presented in our preliminary work [22], but here we explain it from a different perspective to show the DCP generalization. In [1], the DCP-based transmission estimate $\tilde{t}_{rgb}(x) = 1 - \min_{c,y \in \Omega(x)} \left\{ \frac{I^c(y)}{A^c} \right\}$ can also be expressed as:

$$\tilde{t}_{rgb}(x) = \min_{c,y \in \Omega(x)} \left\{ \frac{I^c(y)}{A^c} \right\} = \min_{c,y \in \Omega(x)} \left\{ \frac{A^c - I^c(y)}{A^c} \right\} \tag{8}$$

View Source

The transmission is commonly written as an exponential decay term based on the Beer-Lambert law [30] of light attenuation as $\tilde{t}(x) = e^{-\beta d(x)}$, where $d(x) \geq 0$ is the distance from the camera to the radiant object and β is the spectral volume attenuation coefficient, so $\tilde{t} \geq 0$. In [1], whenever Eq. (8) would yield a negative number (that is, $A^c < I^c(y),\ \forall y \in \Omega(x)$), then $\tilde{t}(x)$ gets clipped to zero. Therefore, scene transmission estimated using Eq. (8) would be inaccurate. To address this, we estimate transmission [22] as:

$$\tilde{t}_{pro}(x) = \max_{c,y\in\Omega(x)} \left(\frac{|A^c - I^c(y)|}{\max(A^c, 1 - A^c)} \right), \tag{9}$$

View Source

where median filtering [3] and linear stretching (to the range $[0.2, \max(\tilde{t}_{pro})]$) are applied to refine the estimated transmission. The intuition behind this expression for $\tilde{t}_{pro}$ is that the numerator captures the absolute difference between the observed intensity and the ambient light, and large values of this quantity correlate with proximity to the camera. That is, observed intensity for close scene points consist more of scene radiance and less of ambient light, and based on Eq. (9), will have large $\tilde{t}_{pro}$. By contrast, observed intensity for a farther scene point consists less of scene radiance and more of ambient light, and $\tilde{t}_{pro}$ is small.

C. Generalization of the DCP

Our approach is a generalization of the DCP-based approaches both for ambient light estimation and transmission estimation. First, consider transmission estimation (Eq. (9)).

1. When the ambient light is bright ($A^c \geq 0.5$) and $A^c \geq I^c,\ c \in \{r, g, b\}$, which holds for many foggy and hazy images, then $\max(A^c, 1 - A^c) = A^c$, so the expression becomes identical to the DCP [1]:

$$\tilde{t}_{pro}(x) = \max_{c,y\in\Omega(x)} \left(\frac{A^c - I^c(y)}{A^c} \right) = \tilde{t}_{rgb}(x). \tag{10}$$

View Source

2. When ambient light is dark ($A^c \leq 0.5$) and $A^c \leq I^c, c \in \{r, g, b\}$, which holds for most dimly lit images, Eq. (9) reduces to the method [24] which uses inverted RGB channels and is meant for night videos:

$$\tilde{t}_{pro}(x) = \max_{c,y\in\Omega(x)} \left(\frac{I^c(y) - A^c}{1 - A^c} \right) = \tilde{t}_{r'g'b'}(x). \tag{11}$$

View Source

3. When $A^r \leq 0.5$ and $A^r \leq I^r$, and $A^k \geq 0.5$ and $A^k \geq I^k,\ k \in \{g, b\}$, which holds for some underwater images where red light is greatly absorbed, Eq. (9) reduces to the method [13] which uses RGB channels with red inverted:

$$\begin{aligned} \tilde{t}_{pro}(x) &= \max_{y\in\Omega(x)} \left(\frac{I^r(y) - A^r}{1 - A^r}, \frac{A^g - I^g(y)}{A^g}, \frac{A^b - I^b(y)}{A^b} \right) \\ &= \tilde{t}_{r'gb}(x). \end{aligned} \tag{12}$$

View Source

4. In [4] and [5], Huang *et al.* found that sometimes images with strong color casts (in which one color channel had a small value in [illegible]). They adopted adaptive gamma correction to try to solve this transmission over-estimation problem. Our general formulation has a solution to this situation as well. For example, when

$I^b \leq A^b \leq 0.5$, and $A^k \geq 0.5$ and $A^k \geq I^k,\ k \in \{r, g\}$, which holds for most sandstorm images where blue light is greatly absorbed by sand, Eq. (9) can be considered as a variant of $\tilde{t}_{rgb}$ [1] which uses the RGB channels with the blue adjusted:

$$\tilde{t}_{pro}(x) = \max_{y \in \Omega(x)} \Big(\frac{A^r - I^r(y)}{A^r}, \frac{A^g - I^g(y)}{A^g}, \Gamma_b \frac{A^b - I^b(y)}{A^b} \Big), \tag{13}$$

View Source

where $\Gamma_b = \frac{A^b}{1 - A^b} \leq 1$ is a multiplicative factor that down weights the blue channel to overcome the over-estimation problem. That is, as A^b gets darker and $I^b \leq A^b$, Γ_b becomes smaller, making the blue channel less important in estimating transmission.

Next, ambient light estimation based on the depth-dependent color change (Eq. (6) and (7)) is a generalization of the DCP-based methods as follows:

1. D reduces to I^{rgb}_{dcp} [1] when $w_c = 1,\ \forall c$ and $\mathbf{s} = 111$, which means that RGB values tend to increase with depth. This is the situation for most hazy images and some underwater images. In such cases,

$$D(x) = \min_{c, y \in \Omega(x)} \big(1 - | \ 1 - I^c(y) \ | \big) = \min_{c, y \in \Omega(x)} I^c(y) = I^{rgb}_{dcp}(x). \tag{14}$$

View Source

2. D reduces to I^{gb}_{dcp} [12] when $w_r = 0, w_g = w_b = 1$ and $\mathbf{s} = -11$ (" – " in $\mathbf{s}$ means don't care), which means that green and blue values tend to increase with depth while red values are ignored in estimating depth. This corresponds to some underwater images where red light is almost completely absorbed. In such cases,

$$D(x) = \min_{y \in \Omega(x)} \{1, 1 - | \ 1 - I^g(y) \ |, 1 - | \ 1 - I^b(y) \ |\} = \min_{c \in \{g, b\}, y \in \Omega(x)} I^c(y) = I^{gb}_{dcp}(x). \tag{15}$$

View Source

3. D reduces to $I^{r'gb}_{dcp}$ [13] when $w_c = 1,\ \forall c$ and $\mathbf{s} = 011$, which means that blue and green values tend to increase with depth while red tends to decrease. This is the situation for most underwater images where red color attenuates more as depth increases. In such cases,

$$D(x) = \min_{y \in \Omega(x)} \{1 - I^r(y), 1 - | \ 1 - I^g(y) \ |, 1 - | \ 1 - I^b(y) \ |\} = I^{r'gb}_{dcp}(x). \tag{16}$$

View Source

4. D reduces to $I^{r'g'b'}_{dcp}$ [23], [24] when $w_c = 1,\ \forall c$ and $\mathbf{s} = 000$, which means that RGB values all tend to decrease as depth increases. This is the situation for most images taken at night with artificial lighting. In such cases,

$$D(x) = \min_{c, y \in \Omega(x)} \{1 - I^c(y)\} = I^{r'g'b'}_{dcp}(x). \tag{17}$$

View Source

D. Radiance Restoration With Adaptive Color Correction

Some input images have color casts which need to be removed in the restoration. If scene radiance is recovered from a degraded image with a color cast using Eq. (5), it often leads to an even stronger color cast. Thus, we incorporate color correction into the IFM. The approach is to adjust ambient light. Based on Eq. (5), we have:

$$J^c(x) = \frac{I^c(x)}{f(x)} - \left[\frac{1}{f(x)} - 1\right] A^c \tag{18}$$

View Source

where $f(x) = \max(\tilde{t}_{rgb}(x), t_0) \in [t_0, 1]$, and $\frac{1}{f(x)} - 1 \geq 0$. Hence, large values in A^c result in small values in J^c and vice versa. Without considering what the "true" ambient light is, if the algorithm assumes a bright ambient light has suffused throughout the observed image, and attempts to restore the image based on that assumption, the resulting restored image will be darker, as the extra brightness is removed, compared to the restoration that would have resulted from an assumption of a dimmer ambient light. An example is shown in Fig. 8 row 1, where as the ambient light is estimated as being brighter, the restored scene radiance gets darker.

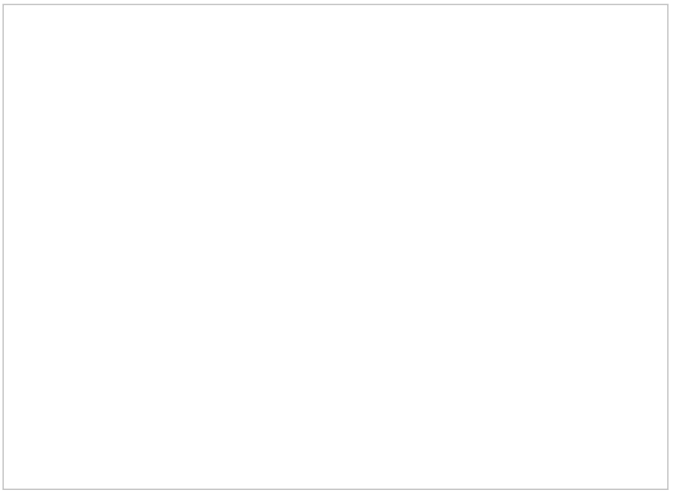

Fig. 8.
Examples of changing hue or brightness of restored scene radiance by adjusting ambient light with given transmission estimated using our method. (a) Original images. (b), (c), and (d) are the restored images using different ambient light. The original images are from [4] and [38].

In the same fashion, a small value in one color channel of the ambient light leads to a substantial increase in that color in the restored image. In Fig. 8 row 2, going from (b) to (c) to (d), the assumed values of the green and blue channels remain constant, but the red value drops from 0.65 to 0.35 to 0.05. As the ambient is assumed to have less red, the restored image based on that assumed ambient has more red. That is, we can adjust the estimate of ambient light based on the input image to remove color casts.

Iqbal *et al.* [28] proposed to keep constant the color channel with the dominant color cast, and scale up the other channels to correct the image color based on the gray world assumption [31]. This approach may suffer from color distortion when there is a strong color cast. Motivated by [28], [29], we calculate color correction coefficients φ^c as

$$\begin{aligned} \varphi^c &= \left\{ \frac{\max_{k\in\{r,g,b\}} I^k_{avg}}{I^c_{avg}} \right\}^{\frac{1}{\sqrt{\max(\xi(I_b),1)}}}, \\ \xi(z) &= \begin{cases} z, & z > \epsilon \\ \infty, & z \leq \epsilon, \end{cases} \end{aligned} \tag{19}$$

View Source

where $I_{avg} = \max(\text{avg}_x I^c(x), 0.1)$. $D_\sigma = \frac{\|\mu_a - \mu_b\|}{\|\sigma\|_2}$ is defined in [29] for measuring the intensity of a color cast, where $\mu = (\mu_a, \mu_b)^T$

represents the means of the chromatic components in the CIELab color space, and $\sigma = (\sigma_a, \sigma_b)^T$ has the chromatic variances. A larger D_σ means a stronger color cast, and $D_\sigma \leq \epsilon$ is taken to mean no color cast, where ϵ is a threshold. Here, we set $\epsilon = 0$. The original work [29] used symmetrical positive and negative thresholds to define regions of color cast, ambiguity, and no color cast, but we simplify this with a single threshold. This choice could be adjusted based on the application (e.g., optimized separately for underwater or sandstorm or haze images).

Then, we adjust the ambient light estimate with $A_\varphi^c = \frac{A^c}{\varphi^c}$. By using A_φ^c in Eq. (5), the estimate of scene radiance is

$$J_\varphi^c(x) = \frac{I^c(x) - A_\varphi^c}{\max\left(\tilde{t}_{pro}(x), t_0\right)} + A_\varphi^c, \tag{20}$$

View Source

where we set t_0 to 0.3. Lower values of t_0 remove more haze but may produce images that are noisy or look less natural, so the exact choice of this parameter depends on the type or purpose of the image. According to Eq. (19), when $D_\sigma \leq \epsilon$, which means there is no color cast, then $\varphi^c = 1$, and $A_\varphi^c = A^c$.

Eq. (19) can be explained in two parts. First we ignore the exponent and consider the quantity $\gamma^c = \frac{\max_{k\in\{r,g,b\}} I_{avg}^k}{I_{avg}^c}$. For an image with a reddish cast, the average red value is larger, so this γ quantity would equal 1 for red and have larger values for blue and green. Using a large value in ambient light produces small values in the restored output whereas a small ambient value leads to an opposite result, so using these γ values in the denominator means that we lower the green and blue ambient values, thus increasing blue and green output scene radiance for color balance. The exponent $\frac{1}{\sqrt{\max(\xi(D_\sigma),1)}}$ aims to avoid color distortion when there is a strong color cast. For example, if a scene shows entirely green plants, D_σ is large because the green color cast is very strong, but one does not want to remove it (of course there are some images with strong color cast that would benefit from color correction). The exponent ensures that as D_σ grows large, φ goes to 1, so there is no color correction.

Fig. 9 shows examples of scene radiance restoration with and without adaptive color correction. The restored images with color correction have more color-balanced results. Therefore, instead of performing color correction on the recovered J , we can achieve both scene radiance restoration and color correction by adjusting the ambient light estimate with the color correction coefficients.

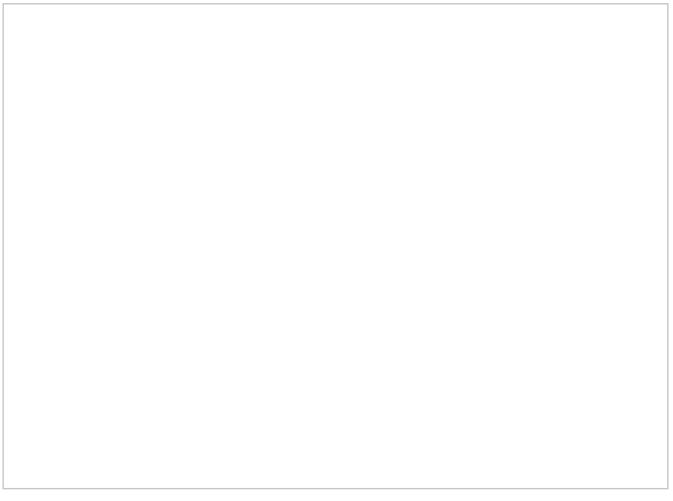

Fig. 9.
Examples of scene radiance restoration with and without adaptive color correction. (a) Original images with estimated ambient light. Restored scene radiance (b) without and (c) with adaptive color correction. The original images are from [5], kkj.cn, and [40].

SECTION IV.
Experimental Results

In this section, we compare our method against various DCP-based restoration methods for foggy, hazy, sandstorm, and underwater images. For terrestrial images, we compare against several state-of-the-art IFM-based image restoration methods described in [4], [5], [17], and [19]. For underwater images, we compare with the methods described in [12] and [14]–[15][16]. First we present a qualitative visual comparison (including transmission maps) and then present objective no-reference quality assessment, and a subjective evaluation using 35 test subjects. At the end of the section, failure cases for our method are discussed.

A. Qualitative Assessment

We show 10 degraded images, including 2 hazy/foggy, 4 sandstorm, and 4 underwater images, with different color tones and lighting conditions. In Fig. 10, the original image is hazy with bright ambient light and does not have a color cast. All methods work well for this case.

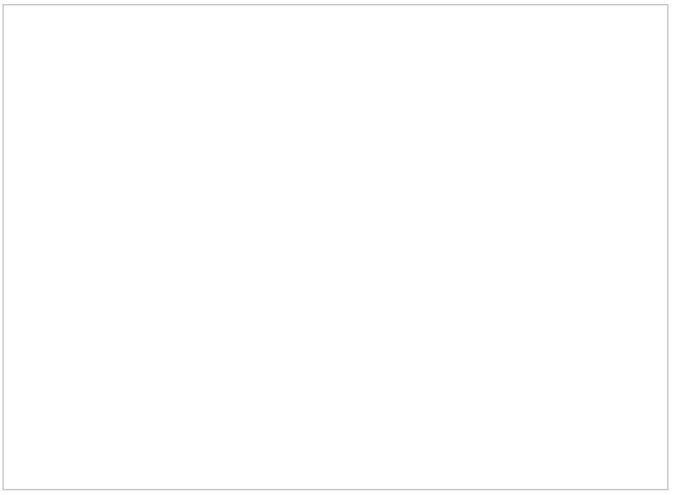

Fig. 10.
Restoration example where all methods are successful. (a) Original image. Restored results and corresponding transmission maps obtained using: (b) [17], (c) [19], (d) [4], (e) [5], and (f) our method. The original image is from [6].

Fig. 11 gives an example of restoring a dark hazy image with a bluish color cast using restoration methods without color correction. The methods [17], [19] barely enhance the contrast of the image because of imprecise transmission estimation for dark hazy images. The processed result using our method has better contrast. Fig. 12 demonstrates more restoration results for the dark hazy image in Fig. 11(a) but using methods with color correction incorporated into the algorithm. The image obtained using [4] presents an even stronger color cast. The method [5] wrongly estimates the entire scene as very close to the camera, leading to negligible restoration. Our method, adjusting ambient light using color correction coefficients $\varphi^c = [1.44, 1.28, 1]$, removes the color cast by magnifying red and green intensities while enhancing contrast.

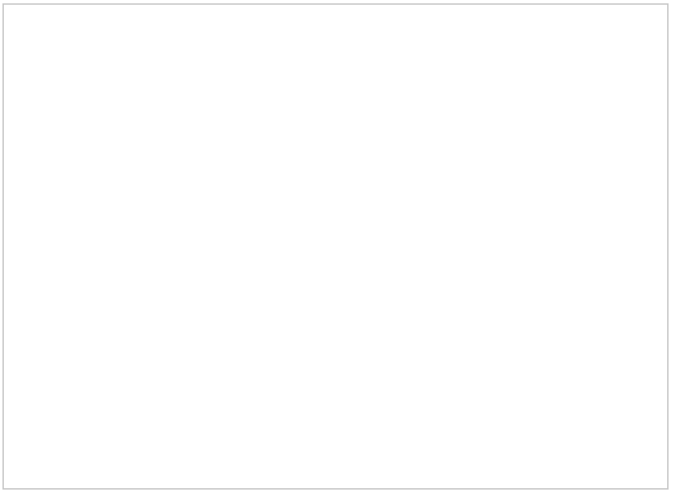

Fig. 11.
An example of restoring a dark hazy image with a color cast. (a) Original image. Restored results and transmission maps obtained using: (b) [17], (c) [19], and (d) our method without color correction ($\varphi^c = 1$). The original image is from [6].

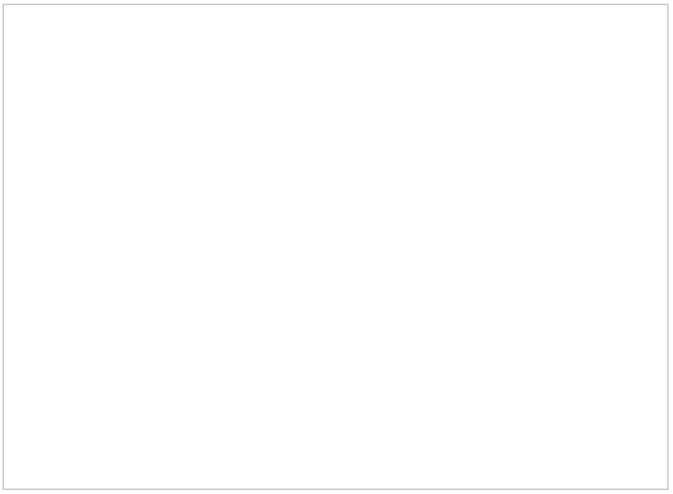

Fig. 12.
Restoring the dark hazy image with a color cast in Fig. 11 (a) using methods with color correction. Restored results and transmission maps obtained using: (a) [4], (b) [5], (c) our method ($\varphi^c = [1.44, 1.28, 1]$).

Fig. 13 shows four sandstorm examples with different color distributions. Based on the histograms of the original images, we consider the images from the first to last row to be shot in progressively thicker sandstorms. In the first row, the scene transmission estimated by [5], [17], and [19] is inaccurate, so their processed images are not sufficiently enhanced. The processed images by our method and [4] both look color corrected, but our method has better contrast.

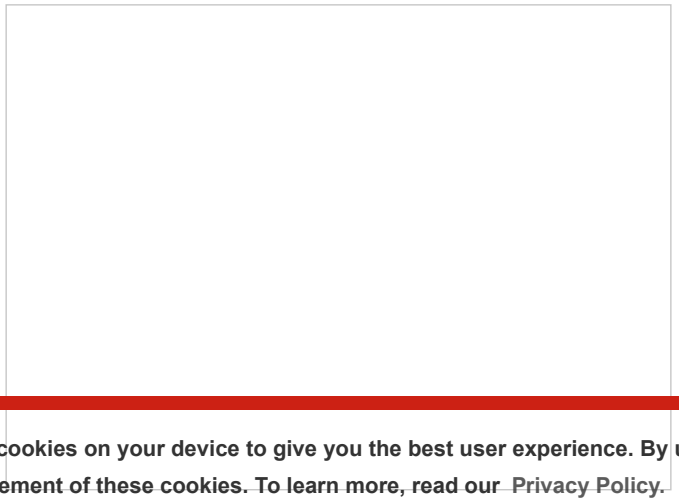

Fig. 13.

Restoring sandstorm images with different color distributions. (a) Original images and their color histograms. Restored results and transmission maps obtained using: (b) [17], (c) [19], (d) [4], (e) [5], and (f) our method. The original images are from [4], [41], and [42]. Note that it is better to view this figure on a screen.

For the second image, the transmission estimated using the methods [17], [19] is wrong, and the restored images are similar to the original. The method [5] fails to enhance contrast of the image and does poorly on color correction. Our method and [4] both correct color while our restored image has better contrast.

For the third image, the processed images obtained using the methods [4], [5], [17] are hardly enhanced. The method [5] does not correct color properly, so the result image looks a little greenish. Although [19] enhances contrast, its color cast problem worsens. Our method is able to produce a better enhanced and color-corrected result. The last original image with a thick sandstorm has very little blue color, which invalidates all the methods except for ours.

Lastly, Fig. 14 demonstrates restoration of underwater images with different color tones and lighting. All methods work well for the first case, and the result images all look restored and enhanced although some color differences exist. The second original image of Fig. 14 is dimly lit, which invalidates the DCP-, MIP-, and MILP-based methods. The processed images by the DCP-based [12], [14], MIP-based [16], and MILP-based [15] methods look insignificantly restored because of the incorrect transmission estimation. Our method generates a much brighter result with more details. The third input image has more blue and green color than red. The processed images from [12], [14], and [16] are negligibly restored because of inaccurate transmission estimation. Although [15] can slightly enhance the contrast of this image, our processed image is more vivid and has better contrast. The last image is very greenish, and the methods [12], [14]–[15][16] only slightly alter the image, whereas our method produces an output with better contrast and more balanced color.

Fig. 14.
Restoring underwater images. (a) Original images. Restored results and transmission maps obtained using: (b) [16], (c) [12], (d) [14], (e) [15], (f) our method. The original images come from [38], and [13]. Note that it is better to view this figure on a screen.

B. Objective Assessment

Image restoration methods can involve objective evaluation [32]–[33] [34][35]. We choose 58 terrestrial images (Fig. 15), with haze, fog, and sandstorm, etc., and use three no-reference image quality metrics. The Natural Image Quality Evaluator (NIQE) [33] uses space domain natural

two, e and r , are blind contrast metrics for which larger values mean better contrast [32]. Table III shows the average e , r and NIQE values for the various restored images of Fig. 15, and our method performs

better. We also choose 55 underwater images (Fig. 16) with different color tones and lighting, and use NIQE and two other no-reference quality metrics, Underwater Image Quality Measure, UIQM [34], and Underwater Color Image Quality Evaluation Metric (UCIQE) [35], for which larger values represent higher quality. Table IV shows average UIQM, UCIQE, and NIQE values of the original images in Fig. 16 and their various restored versions. Our method outperforms the other methods.

TABLE III Average e, $\overline{r}$ and NIQE Values for the Images of Fig. 15 Restored by Various Methods

TABLE IV Average UIQM, UCIQE, and NIQE Values of the Original Images in Fig. 16 and Their Restored Versions From All Methods

Fig. 15.
Terrestrial test images from [1], [4]–[5][6] and Google Images.

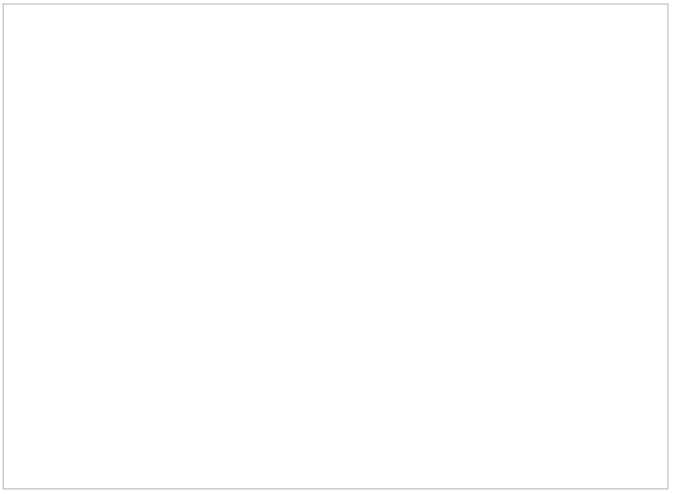

Fig. 16.
Underwater test images from [13], [16], [38] and Google Images.

C. Subjective Evaluation

For the subjective experiment, we pick 25 images from each set (Fig. 15 and Fig. 16). Similar to [36], each method is compared against our method with all possible image pairs generated using the 25 terrestrial and 25 underwater images. There were 35 participants (26 males and 9 females), all of whom are in their twenties or thirties except for one in his forties. The participants were non-experts, consisting of students and a faculty member from UC San Diego. They all have normal or corrected to normal vision.

For each image pair (25×4 pairs for each image set) the subject was asked to choose which image is preferred, or if the images have the same visual quality. The total number of comparisons that each participant performed is 200. All the image pairs shown to each participant were in a random order. For each pair, the images were displayed side by side randomly. Participants could observe an image pair as long as they like before making a choice, but their choice cannot be changed once made.

The results, in Table V, show our method substantially outperforms each of the other methods for both terrestrial and underwater image sets. Average-max-min preference charts are shown in Fig. 17, where we average (and take maximum and minimum values) across participants. So, for each method, the maximum and minimum possible values of the scores for a method are 25 and 0 for a single participant, meaning the participant votes for the method 25 or 0 times. The figure demonstrates our method is highly preferred. In Fig. 18, the chart shows the average percent (over the compared methods) of participants who preferred the proposed method for each terrestrial or underwater image, which further supports that our method is preferred for each image. Note that the images are re-numbered to go from highest average percent to lowest average percent.

TABLE V Subjective Experiment Results. The Numbers Represent How Many Times the Comparison Algorithm or Our Algorithm was Chosen as Preferred, and the Number of Times They were Viewed as Having the Same Quality

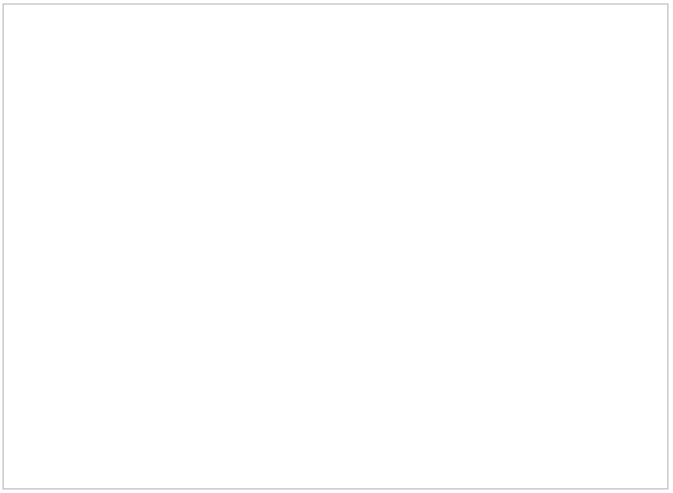

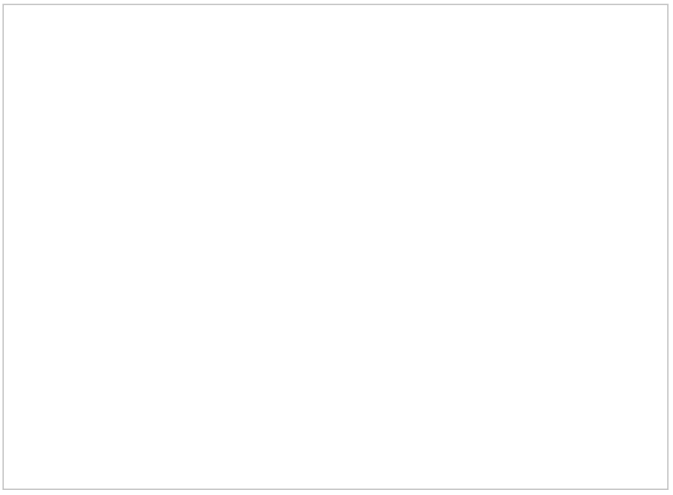

Fig. 17.
Average-max-min preference charts based on all participants for the subjective experiment. (a) Terrestrial images, (b) Underwater images. (Left: The number of times our method was preferred over the comparison methods; Right: number of times compared methods were preferred. Same quality responses are ignored in this figure.)

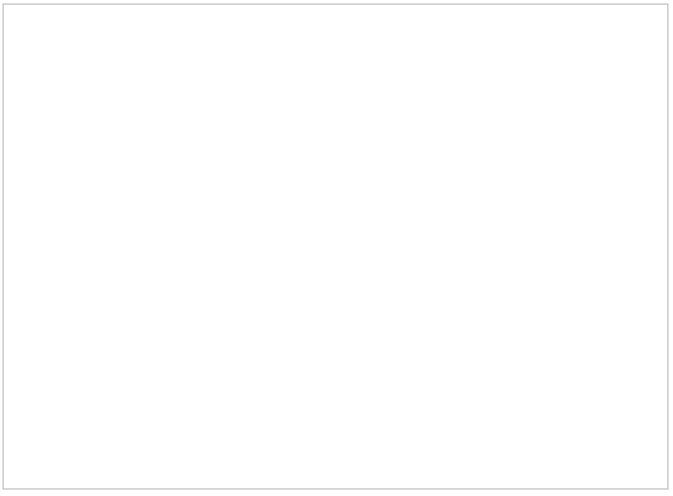

Fig. 18.
The chart shows the average percent (over the compared methods) of participants who preferred the proposed method for each terrestrial/underwater image for the subjective experiment.

D. Failure Cases

As our method is based on the IFM, it fails when the input image cannot be explained by the model. For example, an image with multiple illumination sources may violate the underlying assumption that ambient light is uniform. Fig. 19(a) has light at different depths and cannot be properly restored based on the IFM. Also, our assumption that RGB values tend to increase or decrease roughly linearly with scene

depth does not hold, which leads to wrong ambient light selection (the yellow dot in Fig. 19(a)) and transmission estimation (the second row of Fig. 19(a)).

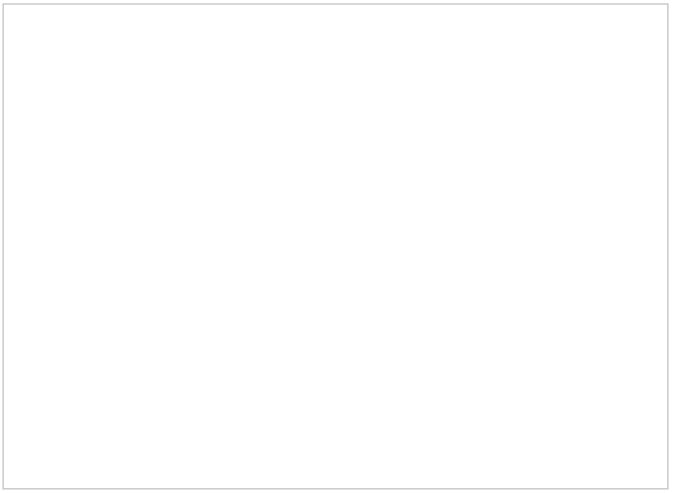

Fig. 19.
Failure cases showing original images and their transmission maps. Yellow dots represent locations from which ambient light is estimated.

To calculate the depth-dependent color change, it is assumed that gradients of far scene points tend to be smaller than those of close scene points. The original image of Fig. 19(b) has sharp edges in both close and far scene points, which violates our assumption and causes the algorithm to fail. So extremely clear water will reduce the validity of the algorithm, but such cases need less restoration in any case.

Other failure cases may arise with large uniform foreground objects. For example, a submarine or ship hull in the foreground may be very smooth with small gradients, and would be wrongly judged as being far away. If it encompassed a small area of the image, it might not be a problem, but if it were sufficiently large, and depending on the object color, it could cause the RGB color change analysis to fail.

SECTION V.
Conclusion

We use the depth-dependent color change, scene ambient light differential, and adaptive color-corrected IFM to better restore degraded images, such as hazy, foggy, sandstorm, and underwater images. We first analyze the depth-dependent color change of the input image to measure scene depth for ambient light estimation. With this estimate, the scene ambient light differential is calculated to estimate scene transmission. Lastly, the input image is restored based on the adaptive color-corrected IFM. Using a wide variety of degraded images with different color tones/casts, contents, and lighting conditions, we demonstrate that our method produces satisfying restored and enhanced results and outperforms other IFM-based methods. Our approach was shown to unify and generalize a wide variety of other DCP-based methods which are aimed at underwater, nighttime, haze, and sandstorm images.

Authors
Figures
References
Citations
Keywords
Metrics